RSC Advances

PAPER

View Article Online
View Journal | View Issue

Cite this: *RSC Adv.*, 2023, **13**, 24053

3D double-reinforced graphene oxide – nanocellulose biomaterial inks for tissue engineered constructs†

Alexandra I. Cernencu,[a] George M. Vlasceanu,*[ab] Andrada Serafim,[a] Gratiela Pircalabioru[cde] and Mariana Ionita *[abc]

Received 27th April 2023
Accepted 13th July 2023

DOI: 10.1039/d3ra02786d

rsc.li/rsc-advances

The advent of improved fabrication technologies, particularly 3D printing, has enabled the engineering of bone tissue for patient-specific healing and the fabrication of *in vitro* tissue models for *ex vivo* testing. However, inks made from natural polymers often fall short in terms of mechanical strength, stability, and the induction of osteogenesis. Our research focused on developing novel printable formulations using a gelatin/pectin polymeric matrix that integrate synergistic reinforcement components *i.e.* graphene oxide (GO) and oxidized nanocellulose fibers (CNF). Using 3D printing technology and the aforementioned biomaterial composite inks, bone-like scaffolds were created. To simulate critical-sized flaws and demonstrate scaffold fidelity, 3D scaffolds were successfully printed using formulations with varied GO concentrations (0.25, 0.5, and 1% wt with respect to polymer content). The addition of GO to hydrogel inks enhanced not only the compressive modulus but also the printability and scaffold fidelity compared to the pure colloid-gelatin/pectin system. Due to its strong potential for 3D bioprinting, the sample containing 0.5% GO is shown to have the greatest perspectives for bone tissue models and tissue engineering applications.

Introduction

Bone tissue's own regeneration ability is adequate for the repair of minor zones of trauma like cracks and certain forms of fracturing, but bone defects that surpass the critical dimension threshold (usually >2 cm, dependent on the anatomical location) will not regenerate without assistance.[1] Currently, developments in nanomaterials synthesis and fabrication, as well as advanced knowledge of bone biology and structure, give fresh prospects for the design of ever more specialized biomaterials for the purpose of bone-tissue engineering (BTE).[2] Conventional bone treatments have been shown to have their shortcomings which can be overcome by three dimensional (3D) printed substrates and it emerged as a promising future strategy for BTE.[3] Scaffold printing has been investigated using a broad variety of natural and synthetic polymers as cell growth promoters among which natural polymers stand out as preferred starting materials.[4] The 3D printing technology is highly reliant on hydrogel inks, either cell-free or cell-loaded, with the appropriate rheological qualities including viscosity, elasticity, and shear-thinning behaviour. However, another significant challenge is still the development of frameworks that fulfil to structural, biomechanical, and osteoconductive criteria for natural bone.[5] Given the lack of sufficient mechanical characteristics that are required by accurate printing and cell-survival throughout the printing process, the development of novel hydrogel-inks or bioinks is attracting considerable interest. In the past decade, graphene and its derivatives were investigated for a variety of applications spanning from catalytic uses to sensing, pharmaceutical systems, and tissue engineering.[6–8] These nanostructured carbonaceous materials offer distinct features where the unique value of graphene in bone restoration is best shown by its mechanical qualities, such as strength, stiffness, or flexibility.[9–11] Furthermore, graphene oxide (GO) provides reactive functional groups that encourage cell attachment and surface chemistry with other compounds.[12] Since GO is unable to offer alone sufficient 3D structuration for large bone defects, polymeric scaffolds containing GO nanomaterials have been proven easier to process and tune to emulate bone microarchitecture.[13] Although they show promise for tissue engineering, 3D graphene composite inks are still in their early stages of research and so far, have been the subject of

[a]*Advanced Polymer Materials Group, University Politehnica of Bucharest, 1-7 Gh. Polizu Street, Bucharest 011061, Romania. E-mail: mariana.ionita@polimi.it*

[b]*Faculty of Medical Engineering, University Politehnica of Bucharest, 1-7 Gh. Polizu Street, Bucharest 011061, Romania. E-mail: george.vlasceanu@upb.ro*

[c]*eBio-hub Research-Center, University "Politehnica" of Bucharest, 6 Iuliu Maniu Boulevard, Campus Building, Bucharest 061344, Romania*

[d]*Research Institute of University of Bucharest, University of Bucharest, Bucharest 050095, Romania*

[e]*Academy of Romanian Scientists, 54 Splaiul Independentei, Bucharest 050094, Romania*

† Electronic supplementary information (ESI) available. See DOI: https://doi.org/10.1039/d3ra02786d

just a limited number of research studies.[14–16] The incorporation of individual GO sheets into organized 3D scaffolds is fundamental to facilitate the wider use of graphene and to develop graphene-based biomaterial inks.[17,18] Several research studies related to GO showed that in combination with cellulose nanostructured materials, in the form of nanocrystals or nanofibers, the stacking effects between GO nanosheets substantially diminishes.[19] Within the context of the strong synergistic interaction between nanostructured cellulose and GO we believe that they are exceptionally well-suited for the development of scalable nanocomposite materials with fascinating emergent features that outperformed graphene alone. Moreover, the potential for employing nanocelluloses in biomedical domains, notably in 3D bioprinting applications, is due to their high surface area, outstanding rheological qualities, biocompatibility, and biodegradability.[20] Recent articles have discussed various nanocellulose-based inks, as well as the benefits and drawbacks of employing cellulosic bioinks for printing vascular tissue, bone, and cartilage, among other biomedical applications (*e.g.*, drug delivery and wound dressings).[21] The majority of the research that has been conducted on nanocellulose-based biomaterials has involved the oxidized form of nanofibrillated cellulose (CNF).[22] Nonetheless, biomaterial ink formulations based on double reinforcement using GO/CNF were not reported in the literature so far. Considering the need of hydrogel matrix, gelatin and pectin, two natural polymers with outstanding biocompatibility and biodegradability, were employed in our research. Gelatin is often employed in tissue engineering research because it contains the arginine-glycine-aspartic acid (RGD) peptide pattern, which promotes cell adhesion, proliferation, and ultimately tissue restoration.[23] Conversely, pectin is a polysaccharide that may be derived from a wide variety of plant sources. Pectin biomaterials are very desirable as delivery vehicles for pharmaceutical and biological species and as scaffolds for tissue regeneration due to their rapid gelation capacity, hydrophilic nature, mucoadhesiveness, and resilience under acidic environments.[24] Both gelatin and pectin are two biopolymers that are often used in medical applications, nevertheless, despite their popularity, they also have major drawbacks.[25–28] For instance, gelatin exhibits a sol–gel transition at physiological temperatures, a fast rate of decomposition and weak mechanical strength that may be detrimental for achieving the standards in BTE. Similar stability issues also exist with pectin, which cannot gel in the absence of chelators and hence destabilizes when introduced to a biological environment. These drawbacks may be avoided, and the strength of both polymers can be improved by chemical crosslinking. A semisynthetic hydrogel component that has shown an outstanding potential for BTE is gelatin methacryloyl (GelMA).[29] GelMA has been used as a suitable matrix for the process of bioprinting bone marrow stromal cells (BMSCs) as well as the bone morphogenetic protein-2 (BMP-2) growth factor and it also has been shown to increase the osteointegration of titanium implants when used as a coating, making it a promising bioink option for BTE.[30] On the other hand, despite its favourable properties, pectin is not yet very popular in designing printable ink and even fewer studies investigate the potential of the methacrylate derivative (PeMA).[31,32] Photocrosslinking is the method of choice since it does not call for the use of any toxic solvents or crosslinking agents, nor does it need high temperatures. By using simple adjustments to the UV radiation dose, polymer concentration, photo-initiator nature and amount, one can easily generate tough and durable photocrosslinked hydrogels, along with cell including versions, with a reasonable degradation rate, high mechanical strength, biocompatibility, *etc.*[33] Since the performance of tissue scaffolding materials is heavily influenced by factors such as rheology, porosity, swelling, mechanical, and biological characteristics, we hypothesized that combining the photocrosslinking abilities of PeMA and GelMA with their intrinsic bioactivity of the GelMA network would enable the production of printable hydrogels with precise control over the afore mentioned characteristics. The double reinforced hydrogels could provide a structural framework for cell cycle progression, and in addition sustain a mechanically suitable environment to enable cell–matrix interactions that guide tissue regeneration. Given the wide range of features required to maximize material performance in the microenvironment, the aim of this study is to develop multicomponent hybrid hydrogels with controlled architecture and high property tunability. Our investigations focused on determining the effect of GO concentration on the rheological behaviour and printability and to assess the overall efficiency of the 3D constructs for bone tissue regeneration. This research contributes to scientific knowledge on GO/CNF hybrid inks which might have far-reaching implications for their use in tissue engineering and regenerative medicine.

Experimental

Materials

Gelatin from fish skin (Sigma-Aldrich-Gelatin from cold water fish skin, BioReagent) was functionalized with methacrylamide side groups in accordance with the protocol outlined in our previous report,[34] where modified gelatin derivative (GelMA) with a methacrylation degree (%MD) of 25% was obtained through the direct reaction of gelatin with methacrylic anhydride in phosphate buffer medium (PBS). Synthesis of pectin functionalized with methacrylate groups (PeMA) was performed by the reaction of pectin (extracted from citrus fruits with low methoxyl content and with a content of galacturonic acid units of 74%, Sigma-Aldrich) with methacrylic anhydride (MA, Sigma-Aldrich) as described elsewhere.[35] Briefly, pectin was dissolved in PBS (pH 7.4) at 1.25%wt/vol and magnetically stirred at room temperature (RT) until complete dissolution. To this solution, MA was added dropwise (0.5 mL min^{-1}) and allowed to react under vigorous stirring. The pH was periodically adjusted to 8.0 by adding 5 M NaOH. After 24 h, the pectin was precipitated in cold acetone (4 °C), followed by freeze-drying. For further purification, the polymer was dissolved in ultrapure water (Millipore) and dialyzed (MWCO 20000, Spectra/Por®, SpectrumLabs) for 5 days. The final product was lyophilized and stored at 12 °C until further use. The degree of methacrylation (DM) was determined by ^{1}H-NMR spectrometry at 31%. More details on determining the DM are explained in the ESI

(Fig. S1†). Carboxylated cellulose nanofibrils (CNF), were generated by subjecting never-dried bleached kraft pulp from softwood (kindly supplied by StoraEnsoTM) to an oxidation process that was TEMPO-mediated, as previously described in ref. 36. Gel-like suspensions of CNF were produced, with a solid content of 1.2% and a degree of modification of 835 mol g^{-1} as determined by conductometric titration.[37] Graphene oxide dispersions in double-distilled water were obtained by sono-chemical exfoliation of GO (powder, 15–20 sheets, 4–10% edge oxidized, purchased from Sigma-Aldrich) under controlled temperature conditions. Briefly, a VCX 750 ultrasonic device from Sonics & Materials, Inc. (Newton, CT, USA) provided with a Ti–6Al–4V probe tip and a 750 W processor operating at 20 kHz in a pulse/pause regime of 30/10 s tip vibrations, at 75% amplitude was used to obtain GO dispersion (15 mL) in sealed beakers placed in ice-cold water baths. In order to maintain the temperature constant, during the 90 minutes exfoliation operation, equal amounts ice were added to the bath every 30 minutes. All other chemicals used were reagent grade and were used as purchased without further purification.

Ink formulation

The preparation of printable formulations with various GO concentrations included redispersing GO in the CNF suspension to achieve GO concentrations of 0.25%, 0.5%, and 1% wt/wt in the CNF-gel (*final GO concentration proportional to mass of polymer in continuous phase). Under magnetic stirring at 37 °C, gelatin methacrylate (GelMA) (8% w/w) was added to the mixture and allowed to dissolve. Then, pectin methacrylate (PeMA) was added at a concentration of 2% w/w and dissolved at 37 °C for 15 minutes. Lithium phenyl-2,4,6-trimethylbenzoylphosphinate (LAP, Sigma Aldrich) was used as photoinitiator and added to the formulation at a concentration of 0.3% wt/vol from a stock solution at 25 mg mL^{-1}. In the following, we will refer to the multicomponent inks as described in Table 1.

Rheology

Rheology data were obtained using a Kinexus Pro rheometer (Malvern Instruments) equipped with a Peltier element for temperature control. To measure the shear viscosity of the precursor suspensions, a plate–plate geometry (20 mm) with a gap of 0.5 mm was used. Viscosity as a function of shear rate was recorded at 37 °C by measurements at constant shear stress in the shear rate interval 0.01 to 1000 s^{-1}. Dynamic oscillatory measurements at 37 °C were also carried out to assess the mechanical properties of the final composite hydrogels. To that purpose, hydrogel samples were prepared in cylindrical moulds and then crosslinked using UV radiation (365 nm, 1 min). A geometry with parallel plates was used, and the samples were positioned on the rheometer's bottom plate before testing. The storage modulus G' and loss modulus G'' were measured in the linear viscoelastic region using oscillatory shear experiments with frequency sweeps ranging from 0.10 to 10 Hz. The average results from three experiments were used to plot the curves.

Table 1 Multicomponent ink formulation

Ink code	GelMA (% w/w)	PeMA (% w/w)	CNF (% w/vol)	GO (% w/w)[a]
GPC_000	8	2	1.2	0
GPC_025	8	2	1.2	0.25
GPC_050	8	2	1.2	0.5
GPC_100	8	2	1.2	1

[a] With respect to polymer concentration.

Printability evaluation and 3D scaffold fabrication

The microvalve-based bioprinting technology was used to carry out the printing experiments and fabricate the scaffolds (3D discovery bioprinter RegenHU, Switzerland). All compositions underwent the 3D printing process at a temperature of 37 °C. A contact microvalve (CF300 ID = 0.3/S = 0.1) and 0.3 mm ID needle (CF300 ID = 0.3/L = 2.4) were utilized to deposit the 3D objects on glass slides using the G-code file and printing protocol generated by BioCAM™ software (Version 1.0, RegenHU). 3D structures designed in the form of discs (d = 15 mm) with 15% lattice infill in 10 layers were manufactured for 3D printing evaluation, while for material testing proportionally smaller discs were fabricated to match testing requirements. The 3D structures were crosslinked by exposing each layer to UV (365 nm) for 5 s. The manufacturing parameters (pneumatic pressure, valve opening time, printing speed) were optimized for each formulation to ensure continuous filament deposition, and further the biomaterial printability as well as the stability of the 3D structures were evaluated.

Compression tests

The 3D printed hydrogels were subjected to compressions using a Brookfield CT3 texture analyser equipped with a 4500 g cell. The samples were printed at the same dimensions ($h \times d$) and subsequently swollen, resulting in specimens with a diameter of $x \pm a$ cm and height of $y \pm b$ cm. The different dimensions of the specimens are due to their hydration; however, the differences between the samples with the same composition were negligible. The measurements were performed in triplicate, at room temperature. The samples were placed on the lower plate of the equipment and subjected to compression at a speed of 0.1 mm s^{-1}. A stress *versus* strain graph was plotted using the dedicated software and the compression modulus (E', kPa) was computed from the slope of the linear part of the compression curve, at 2% strain.

Swelling behaviour

Swelling tests in PBS were used to assess rehydration capacities. Following the weighing of the 3D printed samples to determine the dry mass (W_d), each sample was separately submerged in PBS at room temperature. After withdrawing the samples from the PBS, they were carefully blotted using filter paper, and then immediately weighted to determine the wet weight (W_s) of the samples at various time intervals up to 6 hours. The maximum degree of swelling (MSD) was measured at 24 hours and quantified using the eqn (1). The results of the experiments, which

were carried out in a controlled environment and were repeated for accuracy, were reported as the mean of both sets.

$$\mathrm{MSD}(\%) = \frac{W_s - W_d}{W_d} \times 100 \quad (1)$$

Enzymatic degradation

Composite hydrogels' *in vitro* degradation behaviour was investigated by following the procedure described elsewhere.[38] In short, lyophilized cylindrical samples (10 × 10 mm) were immersed in 0.5 mL of Tris-HCl buffer (0.1 M, pH 7.4) with 0.005% (w/v) NaN_3 and 5 mM CaCl2 at 37 °C. Following an incubation period of one hour, 0.5 mL of a collagenase solution containing 120 U mL^{-1} collagenase dissolved in Tris-HCl buffer was added. Degradation was halted at predetermined time intervals by adding 0.1 mL of 0.25 M EDTA solution, followed by cooling the samples with ice. The hydrogels were then washed three times in ice-cold Tris-HCl buffer for 10 minutes and three times in distilled water for the same amount of time. The gel fraction was calculated by drying the remained hydrogels using the following eqn (2):

$$\mathrm{GF}(\%) = \frac{W_{d,t}}{W_0} \times 100 \quad (2)$$

where the dry mass of the material after it has degraded at time t is denoted by $W_{d,t}$ and the starting weight of the dry sample is denoted by W_0. In this experiment, the data points are represented by the mean and standard deviation of two independent measurements.

Morphology (micro CT)

SkyScan 1272 – high resolution X-ray Microtomograph was employed in the scanning of the four 3D printed objects. Each initial dataset was attained by scanning the freeze-dried prints during a 180° rotation of the object in front of the source (voltage 50 kV, current 170 mA) with a rotation step of 0.2°. Each frame was the result of averaging 4 acquisitions per frame (exposure of 175 milliseconds per projection). For all objects in the batch, the scanning resolution (image pixel size) was set to 10 μm. Tomograms were rebuilt from the raw data using the NRecon software (Bruker). To analyse the tomograms, measure the morphological parameters of the printed objects (total porosity, pore/wall size distribution, *etc.*), and generate the secondary color-coded datasets employed in generating the color-coded scalebar (Fig. 5E), the Bruker CTAn program was used. After thresholding (binarization, whereby only white pixels are used to depict the solid sample and only black pixels for the pores) and despeckling (removal of residual scanning artifacts), all operations performed in order to assess the quantitative features of the samples were conducted based on the conversion of the image pixel size in metric units.

Evaluation of cellular response

The cytocompatibility of the biomaterials was tested on NCTC L929 cells. Cells were cultivated at a density of 10 × 5 cells per well in Dulbecco's modified eagle medium (Gibco) with 10% foetal bovine serum supplemented with penicllin and streptomycin (10 000 U mL^{-1}; Thermo Fisher Scientific). Citotoxicity was measured using the MTT cell proliferation kit (Roche) and the LDH citotoxicity kit (Roche) following the manufacturer's instructions. Absorbance was read at λ = 490 nm using a NanoQuant Infinite M200 Pro instrument. Viability of the cells was analysed using the a live/dead assay (cat. no. L3224). Imaging was performed at λ = 494/517 (live cells) and at λ = 517/617 (dead cells) using a fluorescence microscope (Zeiss AxioScope equipped with an Axiocam 506 mono camera).

Statistical analysis

The measurements were conducted in triplicate ($n = 3$) and the results were plotted as means ± standard deviation *via* GraphPad Prism 6.0 Software (GraphPad Software Inc., version 6.01, 2012, San Diego, CA, USA). The degree of statistical significance has been assessed through the utilization of the same software, employing the one-way ANOVA approach and Bonferroni post-test. A statistical difference was considered to be present when $***p < 0.05$.

Results and discussion

Rheology

Hydrogels' pseudoplastic tendency, in which viscosity drops gradually with increasing shear rate, is a well-known and desired property that enhances printability, allowing for excellent print fidelity. In order to assess the printability of the composite hydrogels and the effect of GO concentration on the formulated inks, the shear stress and viscosity were measured at 37 °C and the data are shown in Fig. 1. The particular rheological properties of printing inks are provided by the multi-component mixtures, where the relationship between shear stress and shear rate shows that the shear stress gradually increases as the shear rate rises. Because nanocellulose combines the features of colloidal gels and nanofibers suspensions, it is mainly responsible for the rheological response of composite formulations.[34,41] In this regard, a major effect over the non-Newtonian behaviour of precursors employing CNF is anticipated in both the low and high shear rate regimes, where the systems show, respectively, solid- and liquid-like features. Linearity is evident in every formulation, but with some very slight curvatures. These are usually characteristic to the weak assembly of the CNF suspension, which may be quickly disrupted by raising the shear rates, but also could be a consequence of surface interactions between CNF and GO. As such, it can be observed that at lowest concentration, a two-step rearrangement occurs: the first negative curvature is attributed to CNF response at increasing the shear rate, while the second one is most likely due to reconfiguration of H-bonding between GO and CNF. Increasing the GO concentration at 0.5%, it was observed that GPC_050 formulation maintains a consistent growing trend even in the high shear rate regime with no significant disruption of the network as a result of the GO loading, which indicates a more stable gel structure

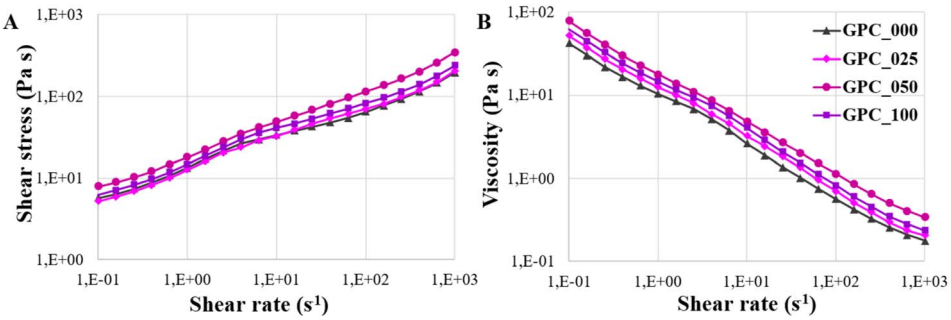

Fig. 1 Shear stress (A) and apparent viscosity (B) as log–log function of shear rates for the composite inks.

formed through (physical) interactions between the hydrogel components. In contrast, with further increasing the GO amount, the curve of GPC_100 formulation exhibited a very similar shape to the one of GPC_000, suggesting a low impact of GO at high concentrations.

The experimental viscosity results reveal that all formulations have a shear – thinning characteristic imparted by CNF, which is the major rationale for adding CNF to the printing precursors. Based on our previous research studies, nanocellulose obviously dominates the formulations' viscosity, and the addition of GelMA and PeMA has little effect on the material's rheological properties.[34,39] Regarding the rheological characteristics of GelMA and PeMA, it is well known in the field of biopolymers that their aqueous solutions behave nearly as Newtonian fluids (particularly at concentrations below 10% wt/wt), where the "n" value is below but close to 1.[40,41] While it is undisputed that $n < 1$ is indicative of shear-thinning fluids, these particular solutions are not suited to 3D printing. In fact, a value of n approximately equal to 0.5 is generally regarded as optimal for this purpose. Although increasing the polymer content increases viscosity proportionally, there are no substantial changes in terms of the slope. The apparent viscosity curves demonstrate that there is a tendency toward a small increase in viscosity with increasing GO concentration. A change in viscosity is noticed over the whole shear rate range with an increase in the GO concentration from 0.25% to 0.50%. Nonetheless, instead of further increasing the viscosity with increasing the amount of GO, at 1% it was observed that the viscosity curve is slightly below the one corresponding to the GPC_050.

Quantitative descriptions of the hydrogels flow behaviour were derived from experimental data obtained *via* rheological characterization. The flow curves have been fitted using the Herschel–Bulkley eqn (3), which is a preferred rheological mathematical model for non-Newtonian fluids data interpretation:

$$\tau = \tau_0 + K\dot{\gamma}^n \quad (3)$$

where τ denotes the shear stress (Pa), τ_0 – the yield shear stress (Pa), K – the consistency index (Pa s^n), $\dot{\gamma}$ the shear rate (s^{-1}) and n the flow behaviour index. Following the regression analysis, the values of n, K, and τ_0 for each hydrogel formulation were determined and presented as tabulated data (Table 2). In order to extrude a material, a certain amount of force is required, and this force is mostly reflected in the dynamic yield stress, τ_0 which is a crucial metric that determines the fluid's flow resistance. Therefore, τ_0 is an intrinsic characteristic that is closely correlated to shear recovery time and consequently to the gel's ability to sustain successive 3D-printed layers.[42] 3D printed structures utilizing materials with a low consistency index are expected to lose shape fidelity gradually with the increase of sequential layers, whereas a low yield stress facilitates smoother extrusion. The determined τ_0 values indicates that all formulations are adequate for 3D bioprinting application, while the value of K indicates a sufficient structural stability. It is interesting to observe that GO has a significant impact over these two parameters and that increasing the amount of GO does not yield in a linear increasing of these values. Based on these parameters, a concentration of 0.5% GO indicates the formation of optimum interactions between ink components that lead to stable network formation. According to the model parameters of the flow curve, the flow index $n < 1$ related to shear-thinning phenomenon, is around 0.48 for all formulations and is practically impartial of the solid content.

The storage and loss moduli for all examined composite hydrogels are displayed in Fig. 2. Hydrogels are characterized by a larger storage modulus (G') than viscous modulus (G''), indicating the gel-like nature of the materials.

Furthermore, the samples exhibit great stability throughout the investigated frequency range (0.1–10 Hz), with no breakdown of cross-link bonds recorded, since G' values are essentially independent of frequency. When the mechanical stability of the CNF-based gels is considered, their distinct rheological behaviour may be completely related to the incorporation of GO. In this regard, it can be observed that the moduli values

Table 2 Rheological parameters of the studied formulations applying Hershel–Bulkley model

Ink code	τ_0 (Pa)	K (Pa s^n)	n	R^2
GPC_000	8.79 ± 2.30	5.90 ± 1.11	0.49 ± 0.02	0.9906
GPC_025	6.57 ± 2.67	7.41 ± 1.40	0.47 ± 0.02	0.9899
GPC_050	8.58 ± 2.86	11.16 ± 1.41	0.48 ± 0.02	0.9931
GPC_100	8.03 ± 2.77	9.41 ± 1.42	0.47 ± 0.02	0.9910

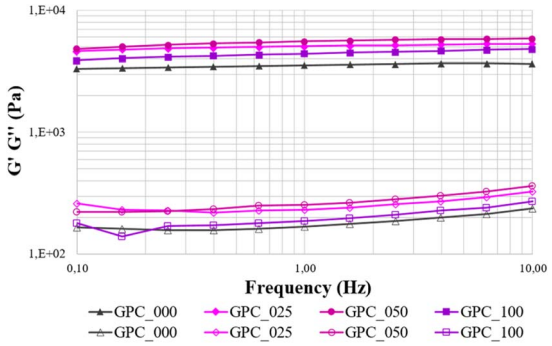

Fig. 2 Elastic and viscous moduli (G' and G'') *versus* frequency for multicomposite hydrogels.

increase with GO concentration up to 0.5% GO, followed by a decrease of the G' value and an increase of the G''. This behaviour might be attributed to a rearrangement of the polymeric entanglements in the presence of a higher amount of GO which further leads to decreased resistance to plastic deformation in GPC_100 when compared to GPC_050 and GPC_025.

Printability evaluation and scaffold 3D fabrication

Shape integrity of the 3D-fabricated scaffold is more likely to be preserved if the ink filaments are continuous, have a smooth shape and are of a consistent thickness. Thus, prior to scaffold 3D printing, experimental trials were conducted to determine the optimal processing parameters (shown in Table 3) and deposition was first evaluated qualitatively to ensure defect-free printing. When employing contact printing (printhead based on microvalve technology), the printing process is primarily controlled by valve opening time (VOT) and valve closing time (VCT) where minimal pressure is necessary. Yet, higher pneumatic pressures are still required for depositing inks with greater viscosity.

In this work, we combine the pressure with extended VOT/VCT to optimize the printing process to lowest pressures for each composition, so that the applied pressure to be below the values that would affect the behaviour of the cells.[43] Both GelMA and PeMA does not exhibit alone sufficient shear recovery to sustain sequential layer deposition and the role of CNF is to aid their printability by imparting a pronounced shear-thinning behaviour.[34,41] 3D scaffolds were printed applying pressures in the range of 30–35 kPa and the variations in VOT/VCT are highly dependable on the rheological behaviour of the inks impacted by the addition of GO. It can be observed that lowest extrusion pressure was used when printing with GPC_025 that also exhibited the lowest yield stress. By comparison with the reference ink, at 0.5% and 1% no significant difference in the external pressure were noticed. Yet, in direct correlation with the consistency index, formulation with higher K values will require longer VOT and VCT times to form continuous filaments. For instance, GPC_050 that exhibit highest K value (11.6 ± 1.41 Pa s^n) requires longest VOT/VCT (1000/2500 μs) in comparison with GPC_000 with a twice lower K value that requires shortest valve timing (800/1800 μs) and no printing delay. A lattice-matrixed 3D model was designed to assess the accuracy with which the composite hydrogels can be printed, and the photographs of printed 3D structures with top view and

Table 3 Printing parameters for GPC composite ink formulations

Ink code	Pressure (kPa)	Feed rate (mm s^{-1})	Valve opening time, VOT (μs)	Valve closing time, VCT (μs)	Dosing distance (μs)	Printing delay (ms)
GPC_000	35 ± 5	10	800	1800	0.1	0
GPC_025	30 ± 2	10	1000	1800	0.1	100
GPC_050	35 ± 4	10	1000	2500	0.1	100
GPC_100	35 ± 2	10	800	2500	0.1	100

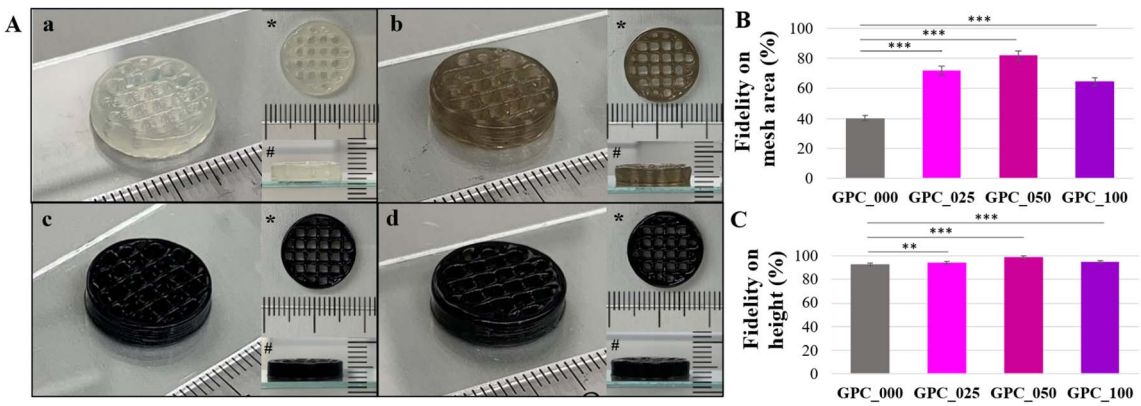

Fig. 3 Photographs of GPC_000 (a), GPC_025 (b), GPC_050 (c) and GPC_100 (d) 3D structures designed as 15 mm discs with 15% lattice filling in 10 layers with top view (*) and side view (#) insets (A); the printing fidelity on mesh area (B) and on height (C).

side view insets are depicted in Fig. 3A. As standardized evaluation grows in importance, 3D modeling a scaffold as a lattice matrix has emerged as the most effective approach. The objective of the 3D design is to ensure an accurate assessment of the printability performance considering the mesh accuracy in terms of macropores shape and area as well as object height while printing small-scale structures. The visual assessment reveals a good printing resolution for all formulation with sufficient structural stability to retain the pre-designed shape and pattern. A qualitative evaluation indicates that GPC_000 exhibits a very good printing resolution, yet by comparison the formulations loaded with GO outperform in terms of print quality. ImageJ was utilized to get accurate measurements of the mesh area and height where parameters describing printing fidelity were calculated according to the method described elsewhere.[44] In brief, the fidelity on mesh area (F_{ma}) was calculated as the ratio between the area of mesh measured in experiments (A_e) and the area of mesh measured on the theoretical 3D model (A_e) as described by eqn (4) and the fidelity on height (F_H) was calculated as the ratio between the printed structure height (H_e) and height measured on the theoretical 3D model (H_t) as described by eqn (5).

$$F_{ma}(\%) = \frac{A_e}{A_t} \times 100 \quad (4)$$

$$F_H(\%) = \frac{H_e}{H_t} \times 100 \quad (5)$$

For each biomaterial composite ink, the printability parameters F_{ma} and F_H were determined and depicted in Fig. 3B and C respectively. The quantitative assessment provided a more accurate comparison between inks printing quality and their potential for the fabrication of scaffolds with controlled architecture. Hence, qualitatively it was observed that the scaffold printed using GPC_000 exhibits a collapse in the filaments overhanging region accordingly, the area of the cavities seems to be reduced, and in some instances the strands are entirely fused. In terms of calculated F_{ma} parameter, the lattice fidelity was calculated at 40%, which is suboptimal for clinically relevant scaffold fabrication. The addition of 0.25% GO significantly improve the fidelity on mesh up to 71% and a further addition of 0.5% GO yields a F_{ma} of 82%. Nonetheless, GPC_100 exhibits a lower lattice print quality of only 65%. With respect to the 3D structures height, all formulations exhibited above 90% fidelity with a similar increasing trend with respect to GO content, where best F_H value was recorded for GPC_050 at 99%. These results indicate that the 0.5% GO concentration establishes optimum components interaction to significantly improve the rheological behaviour in accordance with properties required for high resolution printing.

Compression tests

The compression test is the most straightforward method for determining the general mechanical resistance of hydrogels. This test may be used to determine both the elastic modulus and the shear modulus. In this step, nanocomposite hydrogels based on two biocompatible materials, GelMA and PeMA, were used to synthesize hydrogels, although the primary focus was on determining how the presence of GO and CNF affected the hydrogels' properties. The value of Elastic modulus (E') was calculated at 2% deformation and depicted in Fig. 4 as the mean value of triplicate measurements.

The registered results indicate that the materials' resistance to stress increases with the increase of carbon nanoparticle content, stating for the reinforcing role of GO. In the same time, the plasticizer effect of water present both in the polymeric network and in the pores of the 3D printed specimen must not be overlooked. Unlike the rheology tests, that were performed using un-porous, thin membranes, the compression tests were conducted on porous samples to characterize the scaffolds and not the material itself. The degree of porosity will significantly impact the elastic modulus and induce an interdependent response regarding other properties as well. Given the printing outcomes which involve significant differences between their printing quality, one cannot attain the identical degree of porosity. The compression tests reveal that GPC_100 shows the highest elastic modulus, in contrast with dynamic oscillatory measurements where at 1% GO the hydrogel exhibited decreased resistance to plastic deformation. This result can be explained by the impact of GO on specimen design. In comparison with GPC_025 and GPC_050, GPC_100 exhibits lower microporosity (F_{ma} parameter) – which means a denser scaffold. On the other hand, according to swelling and degradation behaviour, GPC_100 exhibits higher network stiffness. Thus, considering the synergistic effect of these two factors, the effort for GPC_100 sample deformation will be implicitly higher. While the GPC_025 and GPC_050 prove that the addition of GO has a consistent positive impact, the addition of 1% GO could lead to some agglomeration which generates stiff domains. The compression assessment gives an insight on GO impact on mechanical properties considering the also the adjacent factors such as specimen porosity and behaviour in aqueous media. The obtained data suggest that even if the formulations GO_050 and GO_025 have a higher G', when fabricated as 3D scaffolds the composition with the greater amount of GO (GO_100) requires the highest effort to reach the same deformation.

Swelling behaviour

The rehydration characteristics of multicomponent hydrogels were investigated. It has been revealed that the samples

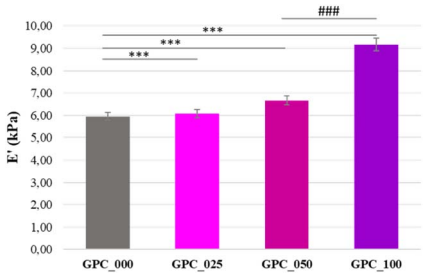

Fig. 4 The modulus of elasticity (E') calculated at a deformation of 2% for the 3D printed hydrogel scaffolds.

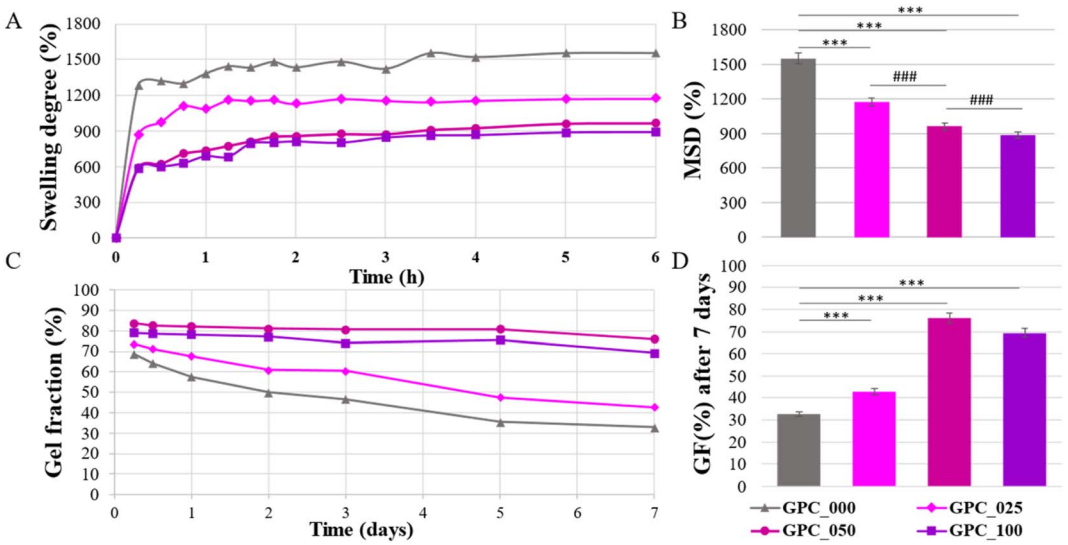

Fig. 5 Swelling kinetics (A) and the maximum degree of swelling (B) in PBS of 3D printed scaffolds, *in vitro* degradation behavior of the hydrogels (C) and the values of gel fraction after 7 days in degrading media (D).

containing the least amount of graphene rehydrate more quickly within the first hour following immersion, in contrast to the samples containing a concentration of 0.5% and 1%, respectively, which display a slower swelling kinetics (Fig. 5A).

However, as graphene concentration increases swelling capacity decreases, with all samples reaching equilibrium in 4 hours. The produced hydrogels exhibit a high swelling capacity, and it is found that the addition of GO at a percentage of 1% greatly effects the swelling capacity of the materials, causing a decrease in the MSD values (1551 ± 54% for GPC_000, 1171 ± 35% for GPC_025, 960 ± 35% for GPC_050 and 886 ± 15 for GPC_100 in Fig. 5B). The findings suggest that the materials have a high degree of hydrophilicity, which is a property that may be attributed to the existence of polymers with a significant hydrophilic character in the continuous phase (GelMA and PeMA). Nonetheless, the presence of GO in the system significantly impacts the swelling behaviour where at only 0.25% GO, a 25% decrease in the MSD was recorded in reference to the GPC_000. It is clear that the incorporation of GO results in the production of a polymer network with increased stiffness.

Enzymatic degradation

The *in vitro* degradation of scaffolds is critical for tissue engineering applications since the degradation behaviour dictates crucial aspects *in vivo*, such as the material's stability and the effectiveness of immobilized bioactive species release. It was hypothesized that the composition of the materials would result in observable and substantial changes in the way they degraded over time. The findings of the *in vitro* degradation investigation of nanocomposite hydrogels are depicted in Fig. 5C and D. Considering the observations of swelling behaviour, the presence of GO would result in a lower degree of deterioration of the nanocomposite systems, and that it would become even less severe as the amount of GO in the precursor formulations increased. The data collected provided evidence in support of this theory, specifically, the multicomponent material containing just 0.25% GO in the formulation displayed a residual GF value of 43% at the end of the degradation testing (7 days). This is equivalent to a nearly complete breakdown of the major constituent (GelMA). Degradation by enzymes was shown to be related to the composition of all tested materials, with a clearly reduced rate of degradation in the presence of a larger quantity of GO. Therefore, the GPC sample with a composition of 0.5% GO has a residual GF of 76%, whereas the GPC_100 sample has a residual GF of 70%.

Morphology (micro CT)

Micro-CT analysis enabled the evaluation of the prints' morphology (printing fidelity, porosity and ink structuration upon freeze-drying) in qualitative and quantitative manner. Fig. 5 depicts the reconstructed tomograms of the four samples. The lowercase subsections (Fig. 6a–d) exhibit the morphology of the square grid model resulted after ink filaments deposition. The square lattice model is preserved throughout the batch, especially in the case of GPC_050. The A–D renderings depict a variation of the morphological features with respect to the width of the solid walls formed during the pore-inducing process. According to this, as the concentration of GO increases, thicker walls seem to emerge. In contrast, the inner pores in the filament lattice widen as the formulation is composited with GO in larger amounts. However, the total porosity of the samples varies insignificantly (within the range of 89.4–90.7%). The isolated slices of the chart represent the solid percentages of the sample, split in two ranges, less than 30 μm and 30–60 μm. Overall, the color-coded representations of walls and pores size distribution was plotted *versus* 30 μm intervals. The predesigned porosity of the CAD model was not considered for this assessment. To begin with, the inner regions, better illustrated in the A–D sections of Fig. 5, are characterized by homogenous walls which seem to differ in

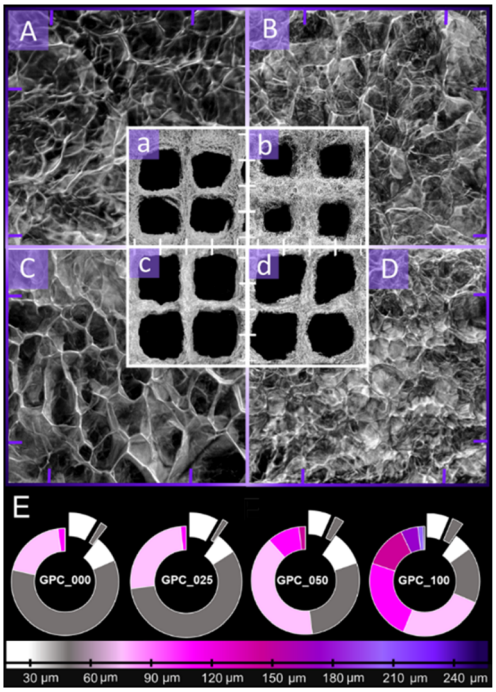

Fig. 6 MicroCT images depicting representative morphology of the 3D printed objects in close-up cross-sectional views ((A) GPC_000, (B) GPC_025, (C) GPC_050 and (D) GPC_100) while the lowercase insets (a–d) illustrate the surface of four-square grids of the infill lattice. The scalebar (distance between two tick marks) is 1 mm for both magnifications. (E) bottom section illustrates the quantitative analysis of pore size within the scanned sample.

terms of solidness as the reinforcing agent concentration is increased.

The homogeneity of the samples is confirmed by the qualitative analysis (Fig. 5E). However, the apparent solidity which is more pronounced in the case of GPC_050 and GPC_100 is rather associated to the tendency of the ink to aggregate in thicker domains, probably because of additional nonbonding interactions of GO with the polymer blend that impact phase separation during the initial stage of freeze drying. Also, such aspects should be addressed paralleled to the distribution of pores formed within the filaments volume. The captured exterior of the printed objects (Fig. 5a–d) indicates the formation of small open pores that are crucial for small molecules exchange with the innermost domains. In the cross-sectional views (A–D), the dense arrangement of walls defines a pore network with a seemingly consistent size distribution; this observation is also supported by the measurement aimed to assess their variability within the printed mesh (excluding the square shaped macropores of the CAD model). Generally, the pore size distributions cover increasingly larger ranges as the GO: polymer ratio is increased; GPC_000 and GPC_025 promote the formation of pores up to 120 μm while in the case of GPC_050 and GPC_100, small shares of ~150 μm and ~250 μm pores are quantified. Furthermore, it can be observed from Fig. 5E that the pore patterning profile of formulations with high reinforcement exhibits a tendency towards achieving equilibrium between domains below and above 100 μm in size, especially for the composite with the highest concentration of GO (marked as gradients of grey – around 50 μm and gradients of purple – around 120 μm). The rather uniform distribution of wall

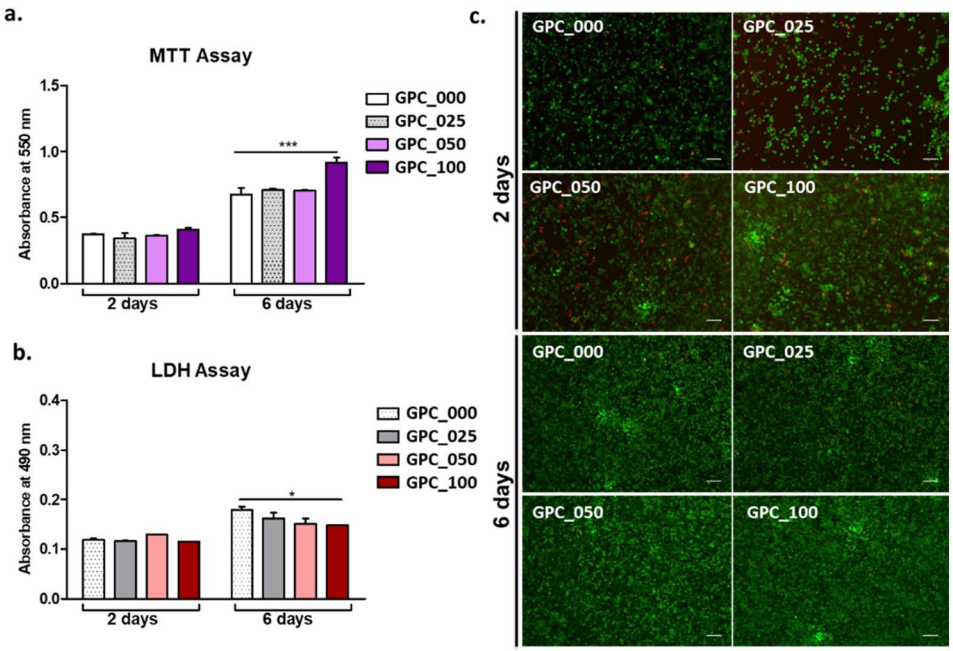

Fig. 7 Biocompatibility assessment of 3D hydrogel scaffolds with L929 murine fibroblasts. (a) Cell viability in contact with scaffolds by MTT assay after 2 and 6 days of culture; (b) GPG cytotoxicity on contact with L929 fibroblasts by lactate dehydrogenase (LDH) assay after 2 and 6 days of culture; (c) live/dead assay of L929 fibroblasts after 2 and 6 days of cultivation; scale bar – 100 μm. *$p < 0.05$; ***$p < 0.001$ by 2-way ANOVA, Bonferroni post-test.

thickness and exterior pore size suggests that these two critical properties were carefully patterned with the GO supplementation, yet without encouraging the growth of unusually big cavities that could weaken the object. Barely any magnitude disparity between the pore system and the walls arises since the incidence of wider pores is counterbalanced by thicker walls that may contribute to the objects' stability.

Evaluation of cellular response

The 3D multicomposites hydrogels were evaluated for biocompatibility against L929 fibroblasts during one week of *in vitro* culture in standard conditions. Biocompatibility assays results showed an overall good biocompatibility of all studied composites cellular viability and proliferation was evaluates quantitatively using 3-(4,5-dimethylthiazol-2-yl)-2,5-diphenyltetrazolium bromide (MTT) (Fig. 7a). After one week of cultivation, cells cultured in contact with the 3D printed scaffolds exhibited a high degree of proliferation. Among the tested composites, the GPC_100 materials displayed a significantly higher viability ($p < 0.001$) compared to the ones cultured in contact with GPC_000 control.

The cytotoxicity of the biomaterials was quantified using the lactate dehydrogenase (LDH) assay after 2 days and 6 days of culture (Fig. 7b). All composites harboured a low level of cytotoxicity after 2 days of culture in standard conditions. Six days after seeding, the levels of released LDH were slightly increased for all tested materials.[45] Among the tested composites, GPC_100 leads to the lowest levels of LDH release, highlighting the high cytocompatibility of this material. Furthermore, the live/dead assay confirmed the quantitative MTT and LDH results, highlighting a strong positive ratio between live (green) and dead (red) cells (Fig. 7c).[45] The overall low degradation rate coupled with aforementioned features indicates that 3D printed scaffolds has a remarkable potential for bone regeneration which require a degradation time-lapse of 24 months.

Conclusions

Recent breakthroughs in nanomaterials synthesis and manufacturing, together with increased understanding of bone biology and structure, have opened exciting new possibilities for the production of more targeted solutions for bone-tissue engineering. Although 3D graphene composite inks have shown promise for tissue engineering, they are still in the early phases of study and have only been the topic of a small number of studies to date. For the purpose of creating scalable nanocomposite materials with remarkable emergent properties that surpass graphene or polymer alone, nanostructured cellulose and GO blends are particularly well-suited and yet, our study is the first to report biomaterial ink formulations based on double reinforcement with GO/CNF. As the performance of tissue scaffolding materials is significantly impacted by parameters such as rheology, porosity, swelling, mechanical, and biological features, we anticipated that the photo-crosslinking abilities of PeMA and GelMA, along with the inherent bioactivity of the GelMA and the structural stability of PeMA, would allow for the fabrication of printable hybrid networks with high perspectives for tissue engineering. The experimental rheological data show that the addition of CNF to the printing precursors imparts a shear – thinning feature to all formulations. The apparent viscosity curves show that when GO content rises, there is a trend toward a little increase in viscosity. As a result of rheological characterization, we were able to acquire quantitative descriptions of the flow behaviour of the hydrogels. GO has a substantial influence on two metrics, yield stress and consistency index, and by increasing the quantity of GO does not result in a linear increase in these values. For these reasons, a concentration of 0.5% GO in the ink suggests the existence of optimal interactions between the components that contribute to stable network development. To evaluate the precision with which composite hydrogels can be printed, 3D scaffolds were fabricated, and it was found that all formulations were capable of producing prints with a high resolution and adequate structural stability to keep the pre-designed shape and pattern. The quantitative analysis allowed for a more precise comparison of the printing performance of various inks, showing that a concentration of 0.5% GO establishes beneficial components interaction, greatly improving the printing resolution in terms of fidelity on mesh area and on height. According to the results of compression tests performed on porous 3D printed scaffolds, by increasing the quantity of GO would likewise increase the effort needed to obtain the same deformation for each sample. The swelling tests clearly reflected that the incorporation of GO results in the production of a polymer network with increased stiffness and that the presence of GO would result in a lower degree of degradation of the nanocomposite systems. The morphology of the composite hydrogels exhibited high porosity with a uniform distribution of pore size upon freeze drying, where thicker walls seem to emerge as the concentration of GO increases. The findings of the cytocompatibility experiments demonstrated a generally adequate level of biocompatibility across all the formulations that were investigated in relation to the MC3T3-E1 cells. The concentration of GO seems to be the most important factor, based on our results, formulations seem to promote cell viability, with increased proliferation occurring when GO concentration is greater than 0.5%. The double-reinforced hydrogels may offer a structural and morphological framework for cell cycle progression while also maintaining a mechanically appropriate environment for cell–matrix interactions that promote tissue regeneration.

Author contributions

Alexandra I. Cernencu: conceptualization, methodology, Investigation, writing – original draft. George M. Vlasceanu: conceptualization, methodology, investigation, writing – review & editing. Andrada Serafim: data curation, investigation. Gratiela Pircalabioru: data curation, investigation. Mariana Ionita: validation, supervision, writing – review & editing.

Conflicts of interest

There are no conflicts to declare.

Acknowledgements

The authors would like to thank for the financial support provided by a grant of the Ministry of Research, Innovation and Digitization, Executive Agency for Higher Education, Research, Development and Innovation, project number PCE 103/2022. This work was also partially supported by a grant from the National Authority for Scientific Research and Innovation, Operational Program Competitiveness under Project No. 154/25.11.2016, P_37_221/2015, SMIS code 108117, GRABTOP.

References

1 G. L. Koons, M. Diba and A. G. Mikos, *Nat. Rev. Mater.*, 2020, **5**, 584–603.
2 M. A. A. Ansari, A. A. Golebiowska, M. Dash, P. Kumar, P. K. Jain, S. P. Nukavarapu, S. Ramakrishna and H. S. Nanda, *Biomater. Sci.*, 2022, **10**, 2789–2816.
3 M. A. Sahebalzamani, M. Ziminska, H. O. McCarthy, T. J. Levingstone, N. J. Dunne and A. R. Hamilton, *Biomater. Sci.*, 2022, **10**, 2734–2758.
4 X. N. Zhang, Q. Zheng and Z. L. Wu, *Composites, B Eng.*, 2022, **238**, 109895.
5 T. D. Ngo, A. Kashani, G. Imbalzano, K. T. Q. Nguyen and D. Hui, *Composites, B Eng.*, 2018, **143**, 172–196.
6 Y. Yang, A. M. Asiri, Z. Tang, D. Du and Y. Lin, *Mater. Today*, 2013, **16**(10), 365–373.
7 J. Li, H. Zeng, Z. Zeng, Y. Zeng and T. Xie, *ACS Biomater. Sci. Eng.*, 2021, **7**(12), 5363–5396.
8 M. Li, D. Sun, J. Zhang, Y. Wang, Q. Wei and Y. Wang, *Biomater. Sci.*, 2022, **10**, 5430–5458.
9 M. Ioniță, G. M. Vlăsceanu, A. A. Watzlawek, S. I. Voicu, J. S. Burns and H. Iovu, *Composites, B Eng.*, 2017, **121**, 34–57.
10 V. B. Mohan, K. tak Lau, D. Hui and D. Bhattacharyya, *Composites, B Eng.*, 2018, **142**, 200–220.
11 S. Huang, Y. Zhong, Y. Fu, X. Zheng, Z. Feng and A. Mo, *Biomater. Sci.*, 2023, **11**, 380–399.
12 A. Lungu, A. I. Cernencu, G. M. Vlasceanu, N. M. Florea, M. Ionita and H. Iovu, *Composites, B Eng.*, 2021, **207**, 108578.
13 D. Ponnamma, Y. Yin, N. Salim, J. Parameswaranpillai, S. Thomas and N. Hameed, *Composites, B Eng.*, 2021, **204**, 108493.
14 M. Silva, I. S. Pinho, J. A. Covas, N. M. Alves and M. C. Paiva, *Funct. Compos. Mater.*, 2021, **2**, 8.
15 J. Li, X. Liu, J. M. Crook and G. G. Wallace, *Front. Bioeng. Biotechnol.*, 2020, **8**, 1–11.
16 G. M. Vlăsceanu, H. Iovu and M. Ioniță, *Composites, B Eng.*, 2019, **162**, 712–723.
17 M. Ionita, A. M. Pandele, L. Crica and L. Pilan, *Composites, B Eng.*, 2014, **59**, 133–139.
18 A. R. Unnithan, C. H. Park and C. S. Kim, *Composites, B Eng.*, 2016, **90**, 503–511.
19 K. Zhang, L. Ketterle, T. Järvinen, G. S. Lorite, S. Hong and H. Liimatainen, *Mater. Des.*, 2020, **193**, 108791.
20 X. Wang, Q. Wang and C. Xu, *Bioengineering*, 2020, **7**, 40.
21 H. Luo, R. Cha, J. Li, W. Hao, Y. Zhang and F. Zhou, *Carbohydr. Polym.*, 2019, **224**, 115144.
22 S. Sultan, G. Siqueira, T. Zimmermann and A. P. Mathew, *Curr. Opin. Biomed. Eng.*, 2017, **2**, 29–34.
23 M. C. Echave, P. Sánchez, J. L. Pedraz and G. Orive, *J. Drug Deliv. Sci. Technol.*, 2017, **42**, 108791.
24 M. C. Teixeira, N. S. Lameirinhas, J. P. F. Carvalho, A. J. D. Silvestre, C. Vilela and C. S. R. Freire, *Int. J. Mol. Sci.*, 2022, **23**, 6564.
25 F. Munarin, M. C. Tanzi and P. Petrini, *Int. J. Biol. Macromol.*, 2012, **51**, 681–689.
26 F. Munarin, S. G. Guerreiro, M. A. Grellier, M. C. Tanzi, M. A. Barbosa, P. Petrini and P. L. Granja, *Biomacromolecules*, 2011, **12**, 568–577.
27 X. Yang, S. Li, Y. Ren, L. Qiang, Y. Liu, J. Wang and K. Dai, *Composites, Part B*, 2022, **237**, 109863.
28 S. Cao, Y. Zhao, Y. Hu, L. Zou and J. Chen, *Composites, Part B*, 2020, **202**, 108445.
29 Z. Dong, Q. Yuan, K. Huang, W. Xu, G. Liu and Z. Gu, *RSC Adv.*, 2019, **9**, 17737–17744.
30 P. S. Zieliński, P. K. R. Gudeti, T. Rikmanspoel and M. K. Włodarczyk-Biegun, *Bioact. Mater.*, 2023, **19**, 292–327.
31 M. Mehrali, A. Thakur, F. B. Kadumudi, M. K. Pierchala, J. A. V. Cordova, M. A. Shahbazi, M. Mehrali, C. P. Pennisi, G. Orive, A. K. Gaharwar and A. Dolatshahi-Pirouz, *ACS Appl. Mater. Interfaces*, 2019, **11**, 12283–12297.
32 J. H. Wang, C. W. Tsai, N. Y. Tsai, C. Y. Chiang, R. S. Lin, R. F. Pereira and Y. C. E. Li, *Int. J. Biol. Macromol.*, 2021, **185**, 441–450.
33 G. Choi and H. J. Cha, *Biomater. Res.*, 2019, **23**, 1–7.
34 A. I. Cernencu, A. Lungu, D. M. Dragusin, I. C. Stancu, S. Dinescu, L. R. Balahura, P. Mereuta, M. Costache and H. Iovu, *Materials*, 2021, **14**, 4891.
35 R. F. Pereira, A. Sousa, C. C. Barrias, P. J. Bártolo and P. L. Granja, *Mater. Horiz.*, 2018, **5**, 1100–1111.
36 A. Lungu, A. I. Cernencu, S. Dinescu, R. Balahura, P. Mereuta, M. Costache, K. Syverud, I. C. Stancu and H. Iovu, *Mater. Des.*, 2021, **197**, 109200.
37 A. Cernencu, A. Lungu, I. C. Stancu, E. Vasile and H. Iovu, *Sci. Bull.–Univ. Politeh. Bucharest, Ser. B*, 2019, **81**, 175–186.
38 G. M. Vlasceanu, L. E. Crica, A. M. Pandele and M. Ionita, *Coatings*, 2020, **10**, 189.
39 A. I. Cernencu, A. Lungu, I.-C. C. Stancu, A. Serafim, E. Heggset, K. Syverud and H. Iovu, *Carbohydr. Polym.*, 2019, **220**, 12–21.
40 M. Zhou, B. H. Lee, Y. J. Tan and L. P. Tan, *Biofabricationm*, 2019, **11**(2), 025011.
41 M. T. Pacheco, M. Villamiel, R. Moreno and F. J. Moreno, *Molecules*, 2019, **24**(3), 392.
42 V. H. M. Mouser, F. P. W. Melchels, J. Visser, W. J. A. Dhert, D. Gawlitta and J. Malda, *Biofabrication*, 2016, **8**, 1–13.
43 K. Fakhruddin, M. S. A. Hamzah and S. I. A. Razak, *IOP Conf. Ser.:Mater. Sci. Eng.*, 2018, **440**.
44 D. Wu, Y. Yu, J. Tan, L. Huang, B. Luo, L. Lu and C. Zhou, *Mater. Des.*, 2018, **160**, 486–495.
45 A. M. Pandele, M. Ionita, L. Crica, S. Dinescu, M. Costache and H. Iovu, *Carbohydr. Polym.*, 2014, **102**, 813–820.